OE Optical Engineering

RESEARCH PAPER

High-precision hyperspectral laser scanning for improved radiometric correction of backscatter intensity

Pabitro Ray,*,† **Tomislav Medić**,*,† **David Salido-Monzú**, and **Andreas Wieser**

Institute of Geodesy and Photogrammetry, ETH Zurich, Zurich, Switzerland

ABSTRACT. Radiometric information offers valuable insights into the surface and material properties of remote targets. Such information can be obtained along with the surface geometry by laser scanning. However, local variations in the surface geometry and orientation can introduce a bias in the radiometric data, related to the angle of incidence (AoI). We demonstrate a supercontinuum-based hyperspectral laser scanning approach for high-precision distance measurements, and its applicability to mitigate the AoI effect by enabling an enhanced data-driven radiometric correction of the acquired intensities. Our experiments utilize a supercontinuum (SC) spectrally broadened to 570 to 970 nm from a 780 nm frequency comb. Distance measurements are derived from the differential phase delay of the intermode beat notes, while the backscattered reflection spectrum is captured using a commercial spectrometer over the spectral range of the SC output. We obtain hyperspectral point clouds with sub-mm range noise on natural targets (gypsum board and leaves of a plant used herein) placed at a distance of 5 m. The high-precision range measurements allow for correctly estimating the surface orientation and modeling the impact of the AoI on the acquired radiometric data. The estimated model is applied to correct the acquired hyperspectral signatures, which are further exploited to compute various vegetation indices commonly used as plant health indicators. Our results illustrate enhanced information content on the direct three-dimensional mapping of such spectral data of plant leaves with a reduced AoI bias. These results highlight new opportunities for future research into remote sensing of vegetation and material probing with increased sensitivity.

 [DOI: 10.1117/1.OE.63.5.054110]

Keywords: hyperspectral LiDAR; frequency combs; supercontinuum; laser scanning; remote sensing; radiometric correction

Paper 20231234G received Dec. 21, 2023; revised May 3, 2024; accepted May 6, 2024; published May 16, 2024.

1 Introduction

Laser scanners are extensively used in several applications, such as industrial manufacturing, surveying, deformation monitoring, and remote sensing, where accurate three-dimensional (3D) geometric acquisition of the environment is essential.[1,2] Commercially available terrestrial laser scanners (TLS) typically use a nearly monochromatic light source. They can already provide sub-mm to cm level accuracy over ranges from a few meters to a few hundred meters, and an estimate of the surface reflectance of the target at the operating wavelength from the captured

*Address all correspondence to Pabitro Ray, pabray@ethz.ch; Tomislav Medić, tmedic@ethz.ch

†Authors contributed equally to this work

backscattered light intensity.[3] This radiometric information is practically useful for material probing and target identification. However, the gathered intensity is influenced by additional factors, such as atmospheric conditions, sensor characteristics, surface properties, stand-off range, and angle of incidence (AoI), which consequently impact the estimated surface reflectance.[4] Traditionally, these effects are compensated by relying on the experimentally obtained calibration functions and direct or derived observations, such as range and surface normals.

Compared to conventionally used monochromatic laser scanners, multi- or hyperspectral laser scanners (HLS) enable capturing the surface geometry of an object along with its spectral characteristics over a wider range of wavelengths. This makes HLS particularly interesting for enhanced target identification and material probing.[5–8] For instance, dual- and multiwavelength solutions that can distinguish plant leaves from wood were shown to be effective for characterizing forest canopy structures.[9,10] Such approaches use a combination of laser sources emitting different wavelengths, where the wavelengths were selected for the specific classification task. An active full-waveform HLS based on a supercontinuum (SC) source is also shown in the literature.[11] The authors used an SC source incoherently broadened from a pulsed laser and spanning from 450 to 1050 nm. A range precision of 11.5 mm over 20 m was achieved using direct time-of-flight measurements on 16 spectral channels within the SC output spectrum. The approach was applied for accurately classifying mineral ores.[12]

The broadband spectrum of the SC offers greater flexibility for selecting the wavelengths and allows extracting further information on the material properties. However, existing HLS technologies show mm to cm level range precision for distances over a few tens of meters.[13,14] This reduced range precision as compared to the established commercial monochromatic instruments directly affects the geometric data quality and derived attributes, such as surface orientation or AoI, which are necessary for effective radiometric calibration. Therefore, enhancing range precision is necessary for obtaining higher-quality structural and radiometric information.

We have recently demonstrated an SC-based HLS approach achieving sub-mm range precision for a stand-off distance up to 50 m.[15] The SC used in our experiments is coherently broadened to 570 to 970 nm from a 780 nm frequency comb. Distance measurements are estimated by monitoring the differential phase delay of the intermode beat notes generated upon direct photodetection of the SC. The spectrum of the light backscattered from the target is acquired using a commercial CCD-based spectrometer with a resolution of 0.16 nm over the SC output spectrum. The developed SC-HLS experimental setup provides high-precision ranging along with pointwise hyperspectral signatures of the scanned scene. A detailed description of the developed experimental setup, and the impact of surface reflectance, data averaging time, and stand-off distance (over 50 m) on the measurement range precision can be found in our earlier work.[15] However, as mentioned earlier, the surface orientation of the scanned object directly influences the acquired radiometric data.

In this paper, we demonstrate how the proposed SC-HLS enables data-driven radiometric correction of intensity measurements for the effect of the AoI. Our method leverages high-precision range measurements to achieve an improved estimation of the surface orientation and AoIs, necessary for mitigating this systematic influence. The latter was not deemed feasible with sufficient accuracy using the existing HLS approaches[16] and was only demonstrated for the cases where AoIs were provided with superior accuracy by additional rotation stage readings acquired at the position of the measured object.[17]

We compare the geometrical quality of our point clouds with those obtained from a structured light scanner (SLS) used for ground-truth measurements and with commercially available state-of-the-art TLSs that employ nearly monochromatic light sources. The range performance of our measurements and the estimated AoIs are comparable to or better than those derived from the commercial instruments and, unlike those, supplemented by hyperspectral signatures at each data point. Relying on the estimated AoIs, we are able to apply a radiometric correction for individual spectral channels and achieve spectral signatures with a reduced AoI bias. We also demonstrate how the corrected hyperspectral data support accurate 3D mapping of vegetation indices (VIs), such as the normalized difference vegetation index (NDVI). Such indices are typically used as plant health indicators and were shown to be sensitive to AoI-related biases.[18] These results highlight the potential of our SC-HLS approach for remote sensing of vegetation. Nevertheless, the

approach can be extended to a broader range of applications involving target identification and material probing.

This paper is structured as follows: Sec. 2 includes a brief description of the measurement principle and the experimental setup. The experimental results in terms of the range performance, radiometric correction, and the derived VIs are presented in Sec. 3. Section 4 summarizes the primary contributions of this work, with directions for further research.

2 Experimental Approach

Figure 1 shows a schematic representation of our experimental setup. We use an SC source coherently broadened (Menlo Systems SCG1500) to a spectral range of 570 to 970 nm using a photonic crystal fiber (PCF) from a 780 nm mode-locked femtosecond laser (Menlo Systems C-fiber 780 SYNC100). The available SC output power is around 26 mW integrated over the entire spectrum. The pulse-repetition rate (f_r) of the mode-locked laser (MLL) is set to 100 MHz, and a rubidium (Rb)-frequency standard (SRS FS725) is used to provide accurate timing references to the MLL and acquisition electronics.

The reflective-type beam expander (RBE) increases the SC output beam to a diameter of 9 mm for better beam collimation over the optical path while minimizing chromatic aberration. A beam sampler (BSF) reflects about 10% of the SC power forming the reference arm, which is subsequently fed to the reference avalanche photodiode ($\mathrm{APD_{ref}}$). The transmitted 90% of the optical power forms the probe arm and passes through the centered hole of an off-axis parabolic mirror (OAP) to reach the scanning mirror (SM). The SM is placed on a programmable two-axis gimbal which allows accurately steering the beam to scan the target specimen. The details of the scanning module and its calibration are described in our previous work.[15] The backscattered light from the target is captured by the OAP and focused onto the $\mathrm{APD_{probe}}$. The -3 dB bandwidth of the APDs used in our experiments is 1 GHz.

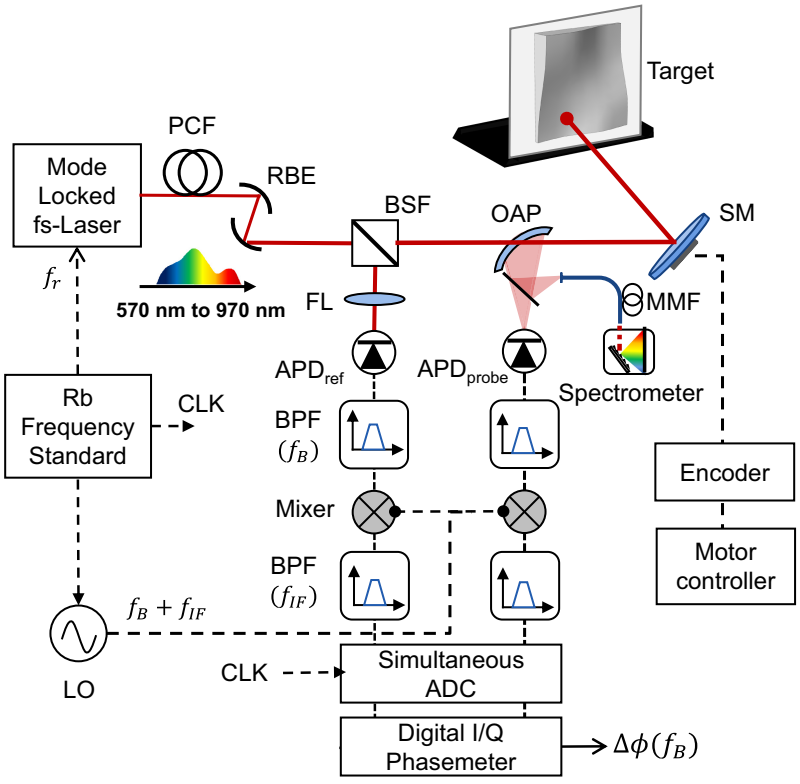

Fig. 1 Schematic representation of the experimental setup (PCF, photonic crystal fiber; RBE, reflective beam expander; BSF, beam sampler; OAP, off-axis parabolic mirror; SM, scanning mirror; FL, focusing lens; APD, avalanche photodiode; MMF, multi-mode fiber; BPF, band-pass filter; LO, local oscillator; CLK, clock; ADC, analog-to-digital converter; I/Q, in-phase/quadrature).

The electrical beat notes generated at the APD are an integer multiple of f_r. Since a higher beat note frequency allows a higher measurement precision,[19] we chose the 10th-harmonic of f_r for distance measurements, i.e., $f_B = 1$ GHz. This choice was limited by the APD bandwidth. The selected beat note f_B is filtered using analog band-pass filters (BPF) centered at 1 GHz and is then downconverted to an intermediate frequency of $f_{\mathrm{IF}} = 400$ kHz before the analog-to-digital conversion (ADC). Both the reference and probe signals are concurrently digitized using a simultaneous-sampling ADC (Spectrum Instrumentation M4i.2234-x8). A digital in-phase/quadrature (I/Q) phasemeter retrieves the differential phase delay between the probe and reference signals, which is then used to estimate the distance to the target. The backscattered light is directed to a commercial CCD-based spectrometer (Thorlabs CCS175) to capture the reflection spectra of the target surfaces. These spectra are recorded with the maximum resolution (0.16 nm) of the spectrometer.

The measured distance (D) is estimated from the differential phase delay between the probe and reference signals, as demonstrated as[15,20]

$$D = \frac{c}{2n_g f_B}\left(\frac{\phi^{\mathrm{probe}} - \phi^{\mathrm{ref}}}{2\pi} + N_M\right). \tag{1}$$

Here, c is the speed of light in vacuum, and n_g is the effective group refractive index estimated using the meteorological conditions in our laboratory on the wavelength obtained through a center-of-mass calculation for the observed optical power spectral density of the SC. The term $(\phi^{\mathrm{probe}} - \phi^{\mathrm{ref}})$ represents the differential phase delay ($\Delta\phi$), accumulated on f_B. Here, N_M denotes the number of round trip range ambiguity cycles, where the range ambiguity is $(c/2n_g f_B)$.

The test specimens used in our experiments are shown in Fig. 2. A rigid 16×16 cm^2 doubly curved smooth surface made of gypsum, Fig. 2(a), is used to assess the range performance of our measurements. The doubly curved surface has a maximum height difference of 2 cm (in the z axis) across its surface. Figure 2(b) shows the different leaves picked from a corn plant (*Dracaena fragrans*) that are used to demonstrate direct 3D mapping of the acquired spectral data and the related derivatives. The leaves chosen herein are from the same plant. However, they partially differ in their size, shape (local curvatures), and radiometric properties, where their visual appearance (green chlorophyll content) and the presence of discolored regions act as health indicators. The leaves are attached to a 40×55 cm^2 large, flat wooden board. The board has been covered by a matte white varnish and provides mechanical stability during the experiments.

All the experiments were conducted under controlled laboratory conditions at 20°C, 955 to 958 hPa, and 50% relative humidity. The fluctuations of the meteorological conditions during our experiments affect the distance measurements with the stand-off range of 5 m by less than about 1 μm and were thus neglected in the data processing. In practical outdoor conditions, the spatial and temporal meteorological variations along the optical path can introduce apparent distance errors of a few mm or more for ranges exceeding a few hundred meters. Traditionally, these refraction-induced distance errors are mitigated by employing a forward modeling-based approach, which involves monitoring the meteorological parameters at the instrument location.[21] If the wavelength-dependent surface penetration and scattering can be distinguished from the

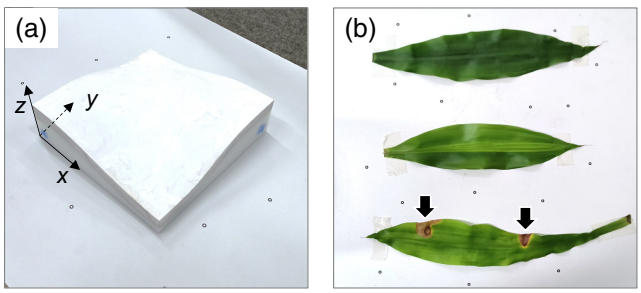

Fig. 2 Pictures of the (a) doubly curved target made of gypsum and (b) the leaves picked from a corn plant (*Dracaena fragrans*, dry leaf spots as indicated by the arrows).

refraction effects, simultaneous measurements on two spectral bands filtered from the SC may also be used to correct the refractivity errors along the optical path, although at the cost of amplified range uncertainty.[22] However, as mentioned earlier, the refractivity error in our experiments is negligible when compared to the achieved scanning range performance over a distance of 5 m.

The measurement output for the i'th point of the scanning module is $(D_i, \vartheta_i, \varphi_i)$, where ϑ and φ are the azimuth and elevation angles of the scanning unit. The captured data are initially converted into 3D Cartesian coordinates $x_{i'}, y_{i'}, z_{i'}$ with the calibrated center of the SM defined as the origin. The targets are placed vertically during measurements (Fig. 1) at the height of the SM with the main surface normal nearly coinciding with the line of sight. For further analysis, $x_{i'}, y_{i'}, z_{i'}$ are transformed into x_i, y_i, z_i with the left bottom corner of the target as the origin, see Fig. 2(a), the z axis approximately parallel to the line of sight at the target center, and the xy-plane vertical in space. The transformation is facilitated by exploiting the known relations (the line of sight vector direction, position, and orientation of the target) between the coordinate systems.

Moreover, the spectrometer acquires the point-wise backscattered light intensity $I'_i(\lambda)$ over the range of wavelengths (λ) of the SC output. The intensity values are affected by the AoI (θ) and other systematic factors, which are not in the focus of this work. In a simplified approximation of the typically used LiDAR model,[17] $I'_i(\lambda)$ can be expressed as

$$I'_i(\lambda) \propto \eta(\lambda) g(D) I_0(\lambda) f_\rho(\lambda, \theta), \tag{2}$$

where $\eta(\lambda)$ is the joint transmission and collection efficiency including the atmospheric and instrumental factors, $g(D)$ describes the dependence on measurement range to the target, $I_0(\lambda)$ is the intensity of the backreflected light at normal incidence, and $f_\rho(\lambda, \theta)$ represents the reflection coefficient (ρ) of the target as a function of θ and λ. The acquired $I'_i(\lambda)$ is normalized to measurements obtained from a common background to eliminate the impact of $\eta(\lambda)$ and $g(D)$ which can be assumed as constant for an instrument at a fixed measurement range. This results in having $(x_i, y_i, z_i, I_i(\lambda))$ information for each scanned point, where $I_i(\lambda)$ is the normalized intensity.

The acquired $I_i(\lambda)$ is processed with a moving Gaussian kernel of 51 points to reduce the high-frequency noise of the individual channels. We chose a spectral range from 600 to 900 nm, taking into account the low signal-to-noise ratio (SNR) outside this range, resulting from the low power at the extreme edges of the SC spectrum available to us. We then subsample the data to a spectral resolution of 1 nm to reduce the number of spectral channels and thereby the computational time required for further analysis. Hence, λ represents the center wavelength of the individual spectral channels from 600 to 900 nm separated by 1 nm, i.e., there are 300 spectral observations in each $I_i(\lambda)$. We correct these hyperspectral signatures radiometrically and show their use for computing VIs, in Secs. 3.2 and 3.3, respectively.

3 Results

3.1 Range Performance

We use the doubly curved gypsum specimen to evaluate the range performance of our measurements. The target specimen was placed at a stand-off range of 5 m. The SC beam hit the specimen approximately parallel to the z axis, see Fig. 2(a), with a maximum deviation of 1.2 deg. For a non-moving beam fixed at a randomly selected position on the target, our measurements show an empirically estimated single-point precision of around 6 μm, evaluated from a time series of 100 measurement points each averaged over a data integration time of 13 ms. The 3D point cloud obtained by scanning the entire target was then compared with those obtained using two state-of-the-art commercial TLSs (Leica ScanStation P50, Z+F Imager 5016) and ground-truth observations from a SLS (GOM Atos Core 300). The measurements using the commercial TLS were also carried out from a stand-off range of 5 m where the expected measurement precision is around 300 μm as per instrument specifications. Due to the relatively short working range (<1 m) of the SLS, the ground-truth measurements were acquired at a stand-off range of only 0.4 m. The expected range precision of these measurements, according to instrument specifications, is at the μm level.

For our experiments, we chose a spatial point spacing of around 3 mm to sample the entire surface of the target. The SLS and TLS data were sub-sampled accordingly to a similar point

spacing. The statistical outlier removal algorithm[23] was applied to eliminate mixed pixels at the surface edges, and other artifacts. We aligned all the point clouds to the coordinate system of our measurements through transformations with 7 degrees of freedom (three translations, three rotations, and scale) by using around 10 corresponding points selected in each dataset. The transformations were necessary for computing the comparable AoIs used in subsequent analyses.

The evaluation of the range performance involved locally fitting a surface using 1% of the total number of data points (26 points for HLS point cloud) within the neighborhood of each point, and computing the range residual of that point with respect to the fitted surface. The surface was approximated by an LOESS[24] regression method using second-order polynomials in the form of

$$z_i = p_1 x_i^2 + p_2 y_i^2 + p_3 x_i y_i + p_4 x_i + p_5 y_i + p_6 + \delta z_i, \tag{3}$$

where $p_{1,\cdots,6}$ are the locally estimated model parameters and x_i, y_i, z_i are the point cloud coordinates as described earlier in Sec. 2. The x_i and y_i are treated as error-free. Given the small angular range covered by the scans, the misfits δz_i are predominantly affected by the measurement range noise and can therefore be interpreted as range residuals. Figure 3(a) shows the computed δz_i obtained from our measurements (SC-HLS), the SLS, and the two TLSs, i.e., TLS^{a} and TLS^{b}.

It can be qualitatively observed from Fig. 3(a) that the range residuals are lower for the SC-HLS measurements than for the commercial TLS^{a,b}. However, they partially exhibit some systematic variations. We expect these to be due to the remaining calibration errors of our scanning module, possibly slightly enhanced by power fluctuations and power-to-phase coupling effects at the APD. This will need to be investigated in the future. Nevertheless, the standard deviation of the residuals is around 4 μm for the SLS, 33 μm for SC-HLS, and around 163 and 178 μm for the two TLSs, thus indicating around five times better performance of the SC-HLS compared to the commercial TLSs at a range of 5 m.

To further assess the SC-HLS performance, the AoI (θ_i) at each data point was calculated as the angle between the line-of-sight and the normal vector of the locally fitted 3D surfaces. We calculated the normal vectors by principal component analysis (as implemented in the point-cloud library[25]), using the five nearest neighbors at each data point. This neighborhood size was chosen as a trade-off between ensuring an adequate level of detail and providing sufficient redundancy for the estimation. The estimated θ_i for the SC-HLS shown in Fig. 3(b) closely resembles the SLS observations and largely represents the actual surface curvature distribution, while the commercial TLSs exhibit notable noise superimposed on the real trends. To quantify the relative deviations, we calculated the difference of the estimated θ_i from the mean value ($\overline{\theta}_i$) within a neighborhood of 10 mm. The standard deviation of $\Delta\theta_i$ for the SLS data are around 0.3 deg, for SC-HLS around 0.7 deg, and for TLS^{a,b} around 3.2 deg. These results indicate the benefits of

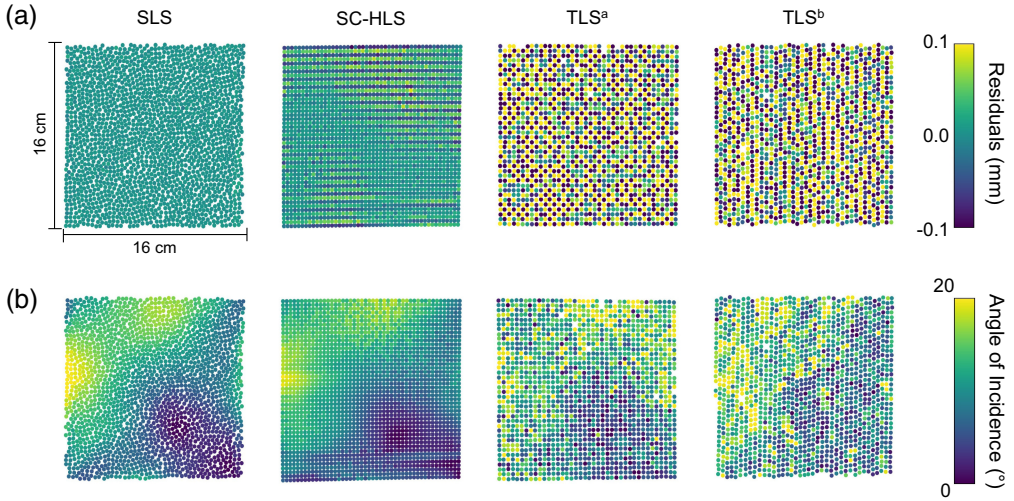

Fig. 3 Comparison of the (a) range residuals and (b) AoIs obtained using different instruments.

high-precision scanning for correctly estimating the surface orientation which can lead to better surface reconstruction and is essential for radiometric correction of the spectral data as shown later in Sec. 3.2.

The relative impact of laser output power and data integration time on measurement precision across the different instruments is not accounted for in this work. For instance, commercial TLS technologies may as well achieve higher precision by adapting the integration time (slower scanning speed) and by using higher laser output power. The focus of this work is on demonstrating a potential solution to achieve precision laser scanning together with hyperspectral information.

3.2 Radiometric Correction

As mentioned earlier, the SC-HLS approach can additionally acquire the reflection spectrum of the target surfaces across the SC output. Existing literature has demonstrated that AoI induces systematic biases in the estimated surface reflectance.[16–18] We carried out further experiments to demonstrate how SC-HLS can be used to reduce the AoI-related dependency on the gathered spectral data.

We acquired both geometrical and spectral information on the plant leaves placed at a range of 5 m using SC-HLS; the target specimen is shown in Fig. 2(b). The geometrical data were also acquired with SLS and TLS for comparison. We used one of the two commercial TLS instruments due to their comparable range performance, as shown in Sec. 3.1. To effectively demonstrate the impact of improved range precision on radiometric correction, relative to the existing HLS systems, we simulated a dataset (HLS^{sim}) exhibiting a higher range noise by adding a zero-mean Gaussian white noise having a standard deviation of 2 mm on our SC-HLS range data. We introduced a quasi-randomly chosen mm-level range noise considering a range precision comparable to or better than that of the existing HLS systems. In this dataset, the contribution of the initial range noise of our measurements can be neglected as it is significantly lower than the simulated noise level (~60 times).

Figure 4 shows the estimated θ_i on the plant leaves for the different datasets. They were computed as described earlier in Sec. 3.1. As compared to the simulated dataset HLS^{sim}, the SC-HLS and TLS measurements exhibit reasonable similarities to the ground-truth observations from the SLS. This is corroborated by evaluating the correlation coefficients with the SLS observations. The SC-HLS and TLS data exhibit a linear correlation coefficient of around 0.4 with the SLS data, whereas HLS^{sim} indicates a value of 0.1.

To analyze the dependency of the measured intensity on AoI [see Eq. (2)], we approximated their relationship by a radiometric correction function based on the combination of Lambertian and Beckmann scattering models for surfaces having both diffuse and specular properties as shown earlier in the literature.[16,17,26] The radiometric correction function can be expressed as

$$I_i(\lambda) = I_0(\lambda) \cdot \left(k_d(\lambda) \cos\,\theta_i + (1 - k_d(\lambda)) \cdot \frac{e^{\frac{\tan^2\theta_i}{m(\lambda)^2}}}{\cos^5\theta_i} \right) + \epsilon_i(\lambda), \tag{4}$$

where $I_0(\lambda)$ is the intensity at normal incidence and $k_d(\lambda)$ is a wavelength-dependent coefficient of the diffuse reflection having a value between 0 and 1. The parameter $m(\lambda)$ is related to the surface roughness of the target, and $\epsilon_i(\lambda)$ is an error term encompassing the random and systematic effects impacting $I_i(\lambda)$ that are not captured through the model in Eq. (4). The term

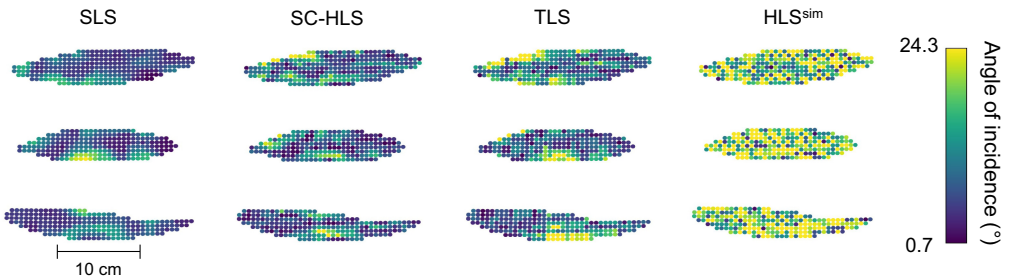

Fig. 4 Comparison of the computed AoI from the point cloud geometry for the different datasets.

$(1 - k_d(\lambda))$ is the coefficient of the specular reflection. The parameters of the correction function were estimated using the robust M-estimator with Tukey's bisquare loss function[27] based on per point $I_i(\lambda)$ and $\theta_i(\lambda)$ values assuming homogeneous surface properties across the leaves; deviations from this assumption are the largest contributors to $\epsilon_i(\lambda)$.

Figure 5 shows the estimated k_d values for each dataset (from Fig. 4). Since the SLS and TLS are monochromatic, we relied on the $I_i(\lambda)$ from SC-HLS for all datasets (related using nearest-neighbor interpolation). The estimated model parameters are affected by the respective θ_i observations and thus indirectly by the range noise. The k_d values derived from the SC-HLS and TLS data closely align with those derived using the geometric ground truth SLS observations. In contrast, the HLS^{sim} data characterized by higher range noise lead to less accurate estimates. The other model parameters (I_0, m) exhibit comparable behavior.

We have determined the median absolute deviation of the estimated model parameters for SC-HLS, TLS, HLS^{sim} data from the reference SLS data, across different λ values. The differences of model parameters estimated from SC-HLS and SLS data are on average 40% lower than those estimated from TLS and SLS data, and 80% lower than the HLS^{sim} and SLS data. Figure 5 further illustrates the wavelength dependency of k_d, which is consistent with the observations previously reported in the literature.[17] Although the spectral indices, often calculated as normalized differences of multiple spectral channels, exhibit reduced sensitivity to the influence of AoI, they cannot entirely eliminate its impact. These results therefore emphasize the necessity for correcting the AoI effect per spectral channel.

Figure 6 shows an example of the correction function estimated using Eq. (4) for the SC-HLS point cloud at $\lambda = 790$ nm. Since the maximum deviation in θ_i is relatively small (<25 deg) in our experiments, it contributes to only a portion of the overall variability within the I_i values, where $R^2 = 0.34$ in Fig. 6(a). Nevertheless, the data after correction shown in Fig. 6(b) indicates that the implemented approach effectively eliminates any noticeable correlation between the I_i and θ_i values.

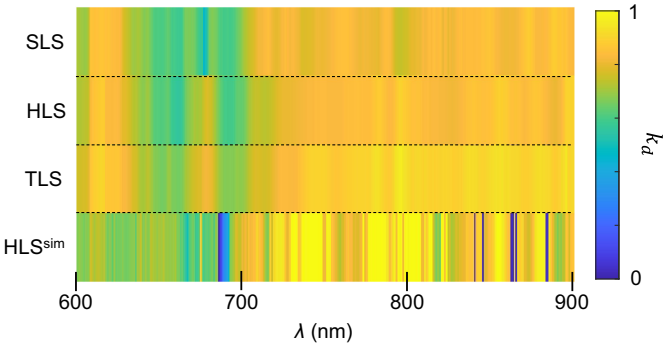

Fig. 5 Comparison of coefficient of diffuse reflection (k_d) estimated from SC-HLS spectrum and geometry data from the various instruments.

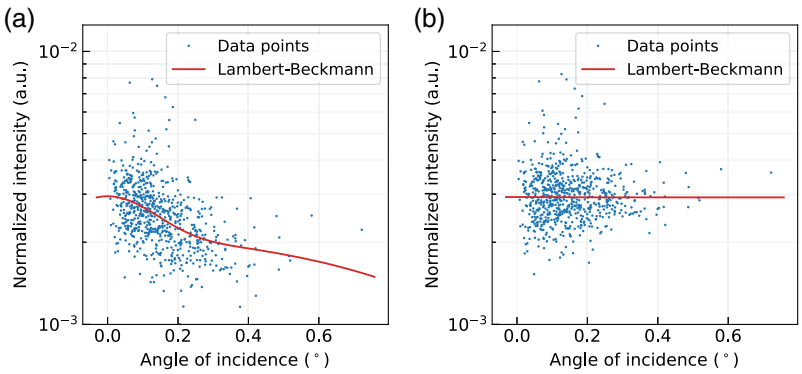

Fig. 6 Normalized intensity observations for 790 nm with the fitted Lambert–Beckmann model (a) before and (b) after radiometric correction.

We further calculated the median absolute deviation of the I_i values before and after applying the correction functions for the respective datasets. Radiometric correction of the SC-HLS data reduced the average variability of I_i values by 23%, compared to 13% for the TLS data. However, the average variability of HLS^{sim} increased by 13%, suggesting that using the correction function based on inaccurate AoI estimates can even introduce further systematic biases rather than eliminating them. These results therefore demonstrate that the improved range precision of our SC-HLS measurements effectively mitigates the AoI-related bias in the acquired spectral data.

3.3 Relevance on the Example of Vegetation Health Monitoring

The hyperspectral signatures offer the flexibility to derive several VIs from a single spectrum. These indices are commonly used as indicators of physiological status related to plant health.[28] Table 1 shows several types of VI calculated from the I_λ observations that fall within the spectral range of our SC, along with a short description of their respective use cases.[28–30] For instance, higher NDVI values indicate a stronger presence of chlorophyll and thus healthier vegetation.

Such indices have a reduced sensitivity to the AoI-related measurement bias, due to partially similar influence on different spectral channels. To eliminate the remaining residual bias, the channel-wise radiometric correction (as described in Sec. 3.2) is applied on I_λ before estimating the VIs. Table 2 shows the correlation values (Spearman's rank correlation) of the calculated VIs with AoI before and after applying the radiometric correction. For instance, the calculated NDVI values are initially significantly correlated ($\rho = 0.36$, $p \ll 0.001$) with the AoI before the radiometric correction. However, after the calibration, the correlation values reduce to $\rho = 0.02$, $p = 0.67$ demonstrating an effective correction. This is also observed for the other VIs (see Table 2), thus confirming that the AoI correction facilitated by the high-precision distance measurements supports the radiometric calibration of the acquired VIs.

Table 1 Investigated VIs with an equation showing the spectral bands used for their computation and relevant use cases. NDVI, normalized difference vegetation index; RVI, simple ratio vegetation index; NDREI, normalized difference red edge index; FRI, fluorescence reflectance index; LCI, leaf chlorophyll index.

VI type	Calculated as	Use cases
NDVI	$(I_{800\text{ nm}} - I_{650\text{ nm}})/(I_{800\text{ nm}} + I_{650\text{ nm}})$	Plant health, nutrition
RVI	$(I_{870\text{ nm}}/I_{660\text{ nm}})$	Plant health, stress-level of crops
NDREI	$(I_{750\text{ nm}} - I_{705\text{ nm}})/(I_{750\text{ nm}} + I_{705\text{ nm}})$	Indicative of mature, ripening crops
FRI	$(I_{600\text{ nm}}/I_{690\text{ nm}})$	Chlorophyll fluorescence
LCI	$(I_{850\text{ nm}} - I_{710\text{ nm}})/(I_{850\text{ nm}} + I_{680\text{ nm}})$	Chlorophyll content

Table 2 Correlation between the different VIs and AoI before and after applying the radiometric correction. Here, ρ is Spearman's rank correlation coefficient, and the associated *p*-value indicates the statistical significance of the observed correlation.

VI type	ρ (before)	*p*-value (before)	ρ (after)	*p*-value (after)
NDVI	0.36	$\ll$0.001	0.02	0.67
RVI	0.44	$\ll$0.001	−0.03	0.44
NDREI	0.15	$\ll$0.001	−0.01	0.80
FRI	0.26	$\ll$0.001	$\ll$0.001	0.95
LCI	0.15	$\ll$.001	−0.02	0.59

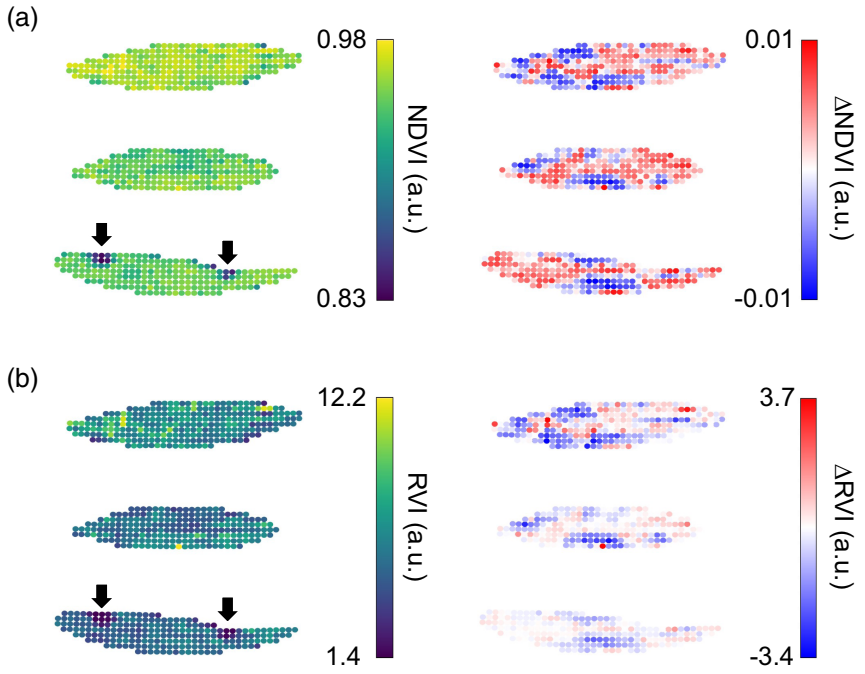

Fig. 7 Point-wise mapping of the (a) NDVI and (b) RVI values calculated using the acquired hyperspectral information, along with their corresponding AoI-related corrections.

This effect is shown in Fig. 7 for NDVI and RVI point-wise mapped onto the acquired point clouds. Figure 7 shows the corrected NDVI and RVI values, along with the differences in their respective observations ΔNDVI, ΔRVI before and after radiometric correction (indicating the associated errors). As anticipated, these differences ΔNDVI, ΔRVI show similar local variations as were observed in Fig. 4 for the AoIs. Although the absolute scale of the respective ΔVI is relatively small in our dataset compared to the VI values, their data spread corresponds to 13% of the overall spread of the NDVI values and 65% for the RVI values.

The calculated VI values also indicate adequate sensitivity to the leaf properties. A higher NDVI is observed for the visibly greener leaves, e.g., the topmost leaf in Fig. 2(b), despite only subtle differences between them in the RGB image. In addition, we also recognize the dry leaf spots by lower NDVI and RVI values, see the marked arrows in Figs. 2(a) and 2(b). These results together highlight the potential of the developed SC-HLS approach for advanced plant health monitoring, which can also be further extended to enhanced material probing.

4 Conclusion and Outlook

We presented a supercontinuum-based hyperspectral laser scanning approach capable of generating high-precision 3D geometrical information of a target with range residuals below 0.04 mm on natural surfaces placed at a range of 5 m. The advantages of precise distance measurements were demonstrated in the context of accurate estimation of the local surface geometry (orientation, surface normal, and AoIs). Our results show a data-driven approach for improved estimation of the surface orientation enabling reduced measurement biases in 3D mapping of spectral data through radiometric correction for the AoI effect, without prior knowledge of the surface orientation. We demonstrated the relevance of the achieved radiometric correction for correctly estimating various plant VIs, such as NDVI, with a reduced AoI-related bias. The developed approach can also be applied for improved material probing and automated point cloud classification.

Code and Data Availability

Data underlying the results will be made publicly available through the ETH Zurich research collection.

Acknowledgments

The present research was co-funded by the Swiss National Science Foundation through research grant 200021_184988 (for P.R.), and by ETH Zurich through a Postdoctoral Fellowship (for T.M.). The authors thank Robert Presl for preparing the target specimens used in this work. Portions of this work were presented at SPIE Optical Metrology in 2023, Proc. 12621.[31]

References

1. M. Amann et al., "Laser ranging: a critical review of usual techniques for distance measurement," *Opt. Eng.* **40**(1), 10–19 (2001).
2. B. Riveiro and R. Lindenbergh, *Laser Scanning: An Emerging Technology in Structural Engineering*, 1st ed., CRC (2019).
3. G. Vosselman and H. Maas, *Airborne and Terrestrial Laser Scanning*, CRC Press (2010).
4. N. Sanchiz-Viel et al., "Radiometric correction of laser scanning intensity data applied for terrestrial laser scanning," *ISPRS J. Photogramm. Remote Sens.* **172**, 1–16 (2020).
5. E. Puttonen et al., "Trees species classification from fused active hyperspectral reflectance and LIDAR measurements," *For. Ecol. Manage.* **260**(10), 1843–1852 (2010).
6. M. Powers and C. Davis, "Spectral LADAR: active range-resolved three dimensional imaging spectroscopy," *Appl. Opt.* **51**(10), 1468–78 (2012).
7. J. Eitel et al., "Beyond 3-D: the new spectrum of lidar applications for earth and ecological sciences," *Remote Sens. Environ.* **186**, 372–392 (2016).
8. Y. Han, D. Salido-Monzú, and A. Wieser, "Classification of material and surface roughness using polarimetric multispectral LiDAR," *Opt. Eng.* **62**(11), 114104 (2023).
9. G. Wei et al., "Multi-wavelength canopy LiDAR for remote sensing of vegetation: design and system performance," *ISPRS J. Photogramm. Remote Sens.* **69**, 1–9 (2012).
10. E. Douglas et al., "Finding leaves in the forest: the dual-wavelength Echidna lidar," *IEEE Geosci. Remote Sens. Lett.* **12**(4), 776–780 (2015).
11. T. Hakala et al., "Full waveform hyperspectral LiDAR for terrestrial laser scanning," *Opt. Express* **20**(7), 7119–7127 (2012).
12. Y. Chen et al., "Feasibility study of ore classification using active hyperspectral LiDAR," *IEEE Geosci. Remote Sens. Lett.* **15**(11), 1785–1789 (2018).
13. B. Chen et al., "Hyperspectral lidar point cloud segmentation based on geometric and spectral information," *Opt. Express* **27**(17), 24043–59 (2019).
14. T. Malkamäki, S. Kaasalainen, and J. Ilinca, "Portable hyperspectral lidar utilizing 5 GHz multichannel full waveform digitization," *Opt. Express* **27**(8), A468–A480 (2019).
15. P. Ray et al., "Supercontinuum-based hyperspectral LiDAR for precision laser scanning," *Opt. Express* **31**(20), 33486–33499 (2023).
16. S. Kaasalainen et al., "Uncertainty in multispectral lidar signals caused by incidence angle effects," *Interface Focus* **8**, 20170033 (2018).
17. W. Tian et al., "Analysis and radiometric calibration for backscatter intensity of hyperspectral LiDAR caused by incident angle effect," *Sensors* **21**(9), 2960 (2021).
18. J. Behmann et al., "Generation and application of hyperspectral 3D plant models: methods and challenges," *Mach. Vision Appl.* **27**, 611–624 (2016).
19. N. R. Doloca et al., "Absolute distance measurement system using a femtosecond laser as a modulator," *Meas. Sci. Technol.* **21**(11), 115302 (2010).
20. P. Ray, D. Salido-Monzú, and A. Wieser, "High-precision intermode beating electro-optic distance measurement for mitigation of atmospheric delays," *J. Appl. Geod.* **17**(2), 93–101 (2023).
21. F. Pollinger et al., "The upgraded PTB 600 m baseline: a high-accuracy reference for the calibration and the development of long-distance measurement devices," *Meas. Sci. Technol.* **23**, 094018 (2012).
22. P. Ray et al., "Refractivity corrected distance measurement using the intermode beats derived from a supercontinuum," *Opt. Express* **32**(7), 12667–12681 (2024).
23. R. Rusu et al., "Towards 3D point cloud based object maps for household environments," *Rob. Auton. Syst.* **56**(11), 927–941 (2008).
24. W. Cleveland and S. Devlin, "Locally weighted regression: an approach to regression analysis by local fitting," *J. Am. Stat. Assoc.* **83**(403), 596–610 (1988).
25. R. Rusu and S. Cousins, "3D is here: Point Cloud Library (PCL)," in *IEEE Int. Conf. Rob. and Autom.* (2011).
26. B. Ginneken, M. Stavridi, and J. Koenderink, "Diffuse and specular reflectance from rough surfaces," *Appl. Opt.* **37**(1), 130–139 (1998).
27. A. Beaton and J. Tukey, "The fitting of power series, meaning polynomials, illustrated on band-spectroscopic data," *Technometrics* **16**(2), 147–185 (1974).

28. J. Penuelas and I. Filella, "Visible and near-infrared reflectance techniques for diagnosing plant physiological status," *Trends Plant Sci.* **3**(4), 151–156 (1998).
29. B. Datt, "Remote sensing of water content in eucalyptus leaves," *Aust. J. Bot.* **47**(6), 909–923 (1999).
30. J. Jia et al., "Hyperspectral LiDAR-based plant spectral profiles acquisition: performance assessment and results analysis," *Remote Sens.* **13**, 2521 (2021).
31. P. Ray et al., "Supercontinuum-based hyperspectral laser scanning: towards enhanced 3D surface reconstruction and its benefits for remote sensing," *Proc. SPIE* **12621**, 126210M (2023).

Pabitro Ray received his doctoral degree from ETH Zurich where he worked on hyperspectral long-distance metrology using a femtosecond laser supercontinuum. His research interests include precision distance metrology, hyperspectral LiDAR, optical sensors, and optoelectronic instrumentation.

Tomislav Medić is a senior scientist in the Institute of Geodesy and Photogrammetry at ETH Zürich. His research interests include sensor error modeling and calibration, geo- and structural health monitoring, LiDAR, point cloud processing, and parameter estimation.

David Salido-Monzú is a senior scientist in the Institute of Geodesy and Photogrammetry at ETH Zürich, working also in sensor technology R&D in industry. His research interests include development around optical metrology, electronic instrumentation, and signal processing, mainly applied to distance measurement, remote material probing, and sensing for electrification.

Andreas Wieser is a full professor of geosensors and engineering geodesy at ETH Zürich. He has more than 20 years of experience in academic research and teaching from various positions held at Vienna University of Technology, Graz University of Technology, and University of Calgary. He also worked in industry as a product manager for GPS-based tolling. His research interests include geodetic monitoring, digitization of reality, LiDAR, parameter estimation, and quality control.